Lagrangian coherent structures and the smallest finite-time Lyapunov exponent

George Haller[1] and Themistoklis Sapsis[2]
[1]*Department of Mechanical Engineering & Department of Mathematics and Statistics, McGill University, 817 Sherbrooke Ave. West, Montreal, Quebec H3A 2K6, Canada*
[2]*Department of Mechanical Engineering, Massachusetts Institute of Technology, 77 Massachusetts Ave., Cambridge, Massachusetts 02139, USA*

(Received 15 April 2010; accepted 29 March 2011; published online 10 May 2011)

We point out that local minimizing curves, or *troughs*, of the smallest finite-time Lyapunov exponent (FTLE) field computed over a time interval $[t_0, t]$ and graphed over trajectory positions at time t mark attracting Lagrangian coherent structures (LCSs) at t. For two-dimensional area-preserving flows, we conclude that computing the largest forward-time FTLE field by itself is sufficient for locating both repelling LCSs at t_0 and attracting LCSs at t. We illustrate our results on analytic examples, as well as on a two-dimensional experimental velocity field measured near a swimming jellyfish. © *2011 American Institute of Physics*. [doi:10.1063/1.3579597]

Lagrangian coherent structures (LCSs) are time-evolving surfaces that act as organizers of trajectory patterns in dynamical systems. The detection of such surfaces from observed or simulated finite-time velocity data sets is important in a number of applications, including atmospheric and oceanic tracer spread analysis. One of the most efficient diagnostic tools for LCSs has been the largest finite-time Lyapunov exponent (FTLE) field, whose ridges appear to mark repelling LCSs. In this note we show that from the same numerical run that generates the forward FTLE field, one can also extract attracting LCSs as troughs of the minimum forward FTLE field graphed over evolving trajectory positions.

I. INTRODUCTION

Lagrangian coherent structures (LCSs), as defined in Haller and Yuan,[5] are distinguished invariant manifolds (*material surfaces*) in the extended phase space of a nonautonomous dynamical system that act as skeletons of patterns formed by trajectories. Specifically, *attracting LCSs over* a time interval $[t_0, t]$ are material surfaces that attract nearby trajectories at the locally highest rate for times $\tau \in [t_0, t]$. As a result of this property, attracting LCSs form the backbones of forward-evolving trajectory patterns over the time interval $[t_0, t]$, acting as central structures on which nearby trajectories accumulate. In particular, attracting LCSs are the theoretical centerpieces of tracer filaments that often form in unsteady fluid flows.

Similarly, *repelling LCSs over* $[t_0, t]$ are material surfaces formed by trajectories of the dynamical system that repel other trajectories at the locally highest rate for times $\tau \in [t_0, t]$. This extreme repulsion causes nearby sets of trajectories to diverge and head toward different regions in the phase space. Specifically, repelling LCSs are the theoretical centerpieces of extreme local stretching regions observed in unsteady flows. As a result, in backward time, repelling LCSs act as attracting material lines.

Haller[6,7] proposed that at time t_0, a repelling LCS over $[t_0, t]$ should appear as a local maximizing curve, or *ridge*, of the finite-time Lyapunov exponent (FTLE) field computed over initial conditions at t_0. Similarly, an attracting LCS $[t_0, t]$ should be a ridge of the backward-time FTLE field. Indeed, ridges of the FTLE field have been broadly found to be accurate indicators of LCSs in a number of applications (see Peacock and Dabiri[11] for a recent review). Haller,[7] however, presents a counterexample and further analysis to show that an FTLE ridge does not necessarily mark the centerpiece of a coherent trajectory pattern. Shadden *et al.*[13] (see also Lekien *et al.*[9]) explore the possibility of *defining* an LCS at t_0 as a ridge of the FTLE field computed over an interval $[t_0, t]$. Realizing that LCSs defined in this fashion are not invariant under the flow, Ref. 9 presents an estimate for the material flux through FTLE ridges. While this estimate turns out to be valid only under further assumptions on the velocity field (cf. Haller[8]), the approach used in Ref. 13 demonstrated, for the first time, the power of differential-geometric tools in exploring features of the FTLE field.

All this work highlighted the potential of FTLE fields in LCS detection, but did not provide a rigorous mathematical link between physically observable LCSs and features of the FTLE field. The recent work of Haller[8] provides such a link through a variational theory that characterizes LCSs as the locally strongest repelling or attracting material surfaces in the flow among all C^1-close material surfaces. This theory provides computable sufficient and necessary criteria for LCSs in terms of invariants of the Cauchy–Green strain-tensor field. Applying these criteria to FTLE ridges yields sufficient and necessary conditions under which an FTLE ridge does mark an LCS. In particular, in two-dimensional flows, an FTLE ridge marks an LCS precisely when it is approximately normal to the eigenvector field associated with the

largest eigenvalues of the Cauchy–Green strain-tensor field (cf. Tang, Chan and Haller[14]).

Currently, the standard way of calculating repelling LCSs at time t_0 is to compute a set of trajectories starting from an array of initial conditions at t_0 up to a time $t > t_0 \geq 0$, then locating the ridges of the forward-time FTLE field from the numerical evaluation of the definition of the FTLE field (cf. below). A separate numerical integration of the dynamical system in backward time from t_0 to $-t$ is required to locate attracting LCSs as ridges of the backward-time FTLE field. Recent numerical techniques for speeding up these calculations appear, e.g., in Brunton and Rowley[2] and Lipinski and Mohseni.[10]

In this brief note, we point out a property of the FTLE field that enables us to compute both attracting and repelling LCSs from a single numerical run. Specifically, while the ridges of largest FTLE computed from t_0 to t mark repelling LCSs at t_0, the minimizing curves (or *troughs)* of the smallest FTLE computed from t_0 to t turn out to mark attracting LCSs at t, when graphed over trajectory positions at time t.

A similar statement holds in backward time: while the ridges of largest FTLE computed from t_0 to $-t$ mark attracting LCSs at t_0, the troughs of the smallest FTLE computed from t_0 to $-t$ turn out to mark repelling LCSs at $-t$, when graphed over trajectory positions at time $-t$.

For two-dimensional flows, further simplifications allow us to use the largest forward-time FTLE to obtain both repelling LCSs at t_0 and attracting LCSs at $t > t_0$. Similarly, the largest backward-time FTLE can be used to locate both attracting LCSs at time t_0 as well as repelling LCSs at $-t$. We illustrate these results on two-dimensional analytical and experimental velocity fields.

In view of Ref. 8, ridges of the smallest and the largest FTLE fields only mark LCS candidates. Further conditions need to be verified on these ridges to ascertain that they are attracting or repelling LCSs, as opposed to spurious structures. Since our focus here is the use of the smallest forward FTLE in detecting LCS candidates, we do not compute the sufficient and necessary LCS conditions derived in Ref. 8. For examples of the use of these conditions, we refer the reader to Refs. 8 and 14.

II. SET-UP AND DEFINITIONS

Consider a dynamical system of the form,

$$\dot{x} = v(x,t), \qquad x \in U \subset \mathbb{R}^n, \qquad t \in [\alpha, \beta], \tag{1}$$

with a smooth vector field $v(x, t)$ defined on the n-dimensional open domain U over a time interval $[\alpha, \beta]$.

At time t, a trajectory of system (1) is denoted by $x(t, t_0, x_0)$, starting from the initial condition x_0 at time t_0. The *flow map* $F_{t_0}^t(x_0)$ maps the initial position x_0 of the trajectory into its position at time t,

$$F_{t_0}^t : U \to U, \tag{2}$$
$$x_0 \mapsto x(t, t_0, x_0).$$

By fundamental results from the theory of ordinary differential equations (see Arnold[1]), the flow map is as many times differentiable in x_0 as is $v(x, t)$ in x. In particular, if $v(x, t)$ is continuously differentiable, then we can use the deformation gradient $DF_{t_0}^t(x_0)$ to define a classic measure of strain, the *right Cauchy–Green strain tensor* $C_{t_0}^t(x_0)$ as

$$C_{t_0}^t(x_0) = \left[DF_{t_0}^t(x_0)\right]^T DF_{t_0}^t(x_0), \tag{3}$$

with the superscript T referring to matrix transposition.

We note that the *left Cauchy–Green strain tensor* $B_{t_0}^t(x_0)$ can be analogously defined as

$$B_{t_0}^t(x_0) = DF_{t_0}^t(x_0)\left[DF_{t_0}^t(x_0)\right]^T. \tag{4}$$

With $C_{t_0}^t(x_0)$ at hand, the *largest FTLE* associated with the trajectory $x(t, t_0, x_0)$ over the time interval $[t_0, t]$ is defined as

$$\begin{aligned}\Lambda_{t_0}^t(x_0) &= \frac{1}{|t-t_0|}\log ||DF_{t_0}^t(x_0)|| \\ &= \frac{1}{|t-t_0|}\log \sqrt{\lambda_{\max}\left[C_{t_0}^t(x_0)\right]},\end{aligned} \tag{5}$$

where $||DF_{t_0}^t(x_0)||$ denotes the operator norm of $DF_{t_0}^t(x_0)$. This norm is equal to the square root of $\lambda_{\max}\left[C_{t_0}^t(x_0)\right]$, the largest eigenvalue of $C_{t_0}^t(x_0)$. Since $C_{t_0}^t$ is a symmetric and positive definite tensor by definition, the largest eigenvalue used in (5) is always real and positive.

For later reference, we also define here the *smallest* FTLE associated with the trajectory $x(t, t_0, x_0)$ over the time interval $[t_0, t]$ as

$$\Gamma_{t_0}^t(x_0) = \frac{1}{|t-t_0|}\log \sqrt{\lambda_{\min}\left[C_{t_0}^t(x_0)\right]}, \tag{6}$$

with $\lambda_{\min}[C_{t_0}^t(x_0)]$ referring to the smallest eigenvalue of $C_{t_0}^t(x_0)$. The smallest FTLE (6) does not naturally arise in measuring the growth of infinitesimal perturbations along $x(t, t_0, x_0)$. For this reason, the connection between $\Gamma_{t_0}^t$ and LCSs has remained unexplored.

III. LARGEST BACKWARD-TIME FTLE FROM THE SMALLEST FORWARD-TIME FTLE

A. General case

The following simple relationship can be deduced from the above definitions:

Proposition 1: Consider the times $t > t_0 \geq 0$. Then the largest FTLE computed from t to t_0 at the location $x_t = F_{t_0}^t(x_0)$ is equal to the negative of the smallest FTLE computed from t_0 to t at the initial condition x_0. Specifically, we have

$$\Lambda_t^{t_0}(x_t) = -\Gamma_{t_0}^t(F_t^{t_0}(x_t)). \tag{7}$$

Proof: By definition, the largest FTLE computed from time t to t_0 at the location x_t is given by

$$\Lambda_t^{t_0}(x_t) = \frac{1}{|t_0 - t|} \log \sqrt{\lambda_{\max}\left[C_t^{t_0}(x_t)\right]}. \tag{8}$$

To compute the right Cauchy–Green strain tensor

$$C_t^{t_0}(x_t) = \left[DF_t^{t_0}(x_t)\right]^T DF_t^{t_0}(x_t), \tag{9}$$

we note that, by the chain rule, we have $DF_t^{t_0}(x_t)\, DF_{t_0}^t(x_0) = I$, or, equivalently,

$$DF_t^{t_0}(x_t) = \left[DF_{t_0}^t(x_0)\right]^{-1}. \tag{10}$$

Substituting (10) into (9), we obtain

$$\begin{aligned} C_t^{t_0}(x_t) &= \left[\left[DF_{t_0}^t(x_0)\right]^{-1}\right]^T \left[DF_{t_0}^t(x_0)\right]^{-1} \\ &= \left[\left[DF_{t_0}^t(x_0)\right]^T\right]^{-1} \left[DF_{t_0}^t(x_0)\right]^{-1} \\ &= \left[DF_{t_0}^t(x_0)\left[DF_{t_0}^t(x_0)\right]^T\right]^{-1} \\ &= \left[B_{t_0}^t(x_0)\right]^{-1}. \end{aligned} \tag{11}$$

Therefore, the right Cauchy–Green strain tensor computed from t to t_0 at point x_t is just the inverse of the left Cauchy–Green strain tensor computed at the point x_0 from time t_0 to t. Formula (11) implies

$$\lambda_{\max}\left[C_t^{t_0}(x_t)\right] = \frac{1}{\lambda_{\min}\left[B_{t_0}^t(x_0)\right]}. \tag{12}$$

Next we note that the eigenvalues of $B_{t_0}^t$ coincide with those of $C_{t_0}^t$. Indeed, if λ is an eigenvalue of $B_{t_0}^t$ with eigenvector e, then we have

$$DF_{t_0}^t\left[DF_{t_0}^t\right]^T e = \lambda e,$$

which, after left-multiplication by $\left[DF_{t_0}^t\right]^T$, yields

$$C_{t_0}^t\left[DF_{t_0}^t\right]^T e = \lambda\left[DF_{t_0}^t\right]^T e,$$

implying that $\left[DF_{t_0}^t\right]^T e$ is an eigenvector of $C_{t_0}^t$ with eigenvalue λ.

We conclude that $\lambda_{\min}\left[B_{t_0}^t(x_0)\right] = \lambda_{\min}\left[C_{t_0}^t(x_0)\right]$ holds, thus (12) gives

$$\lambda_{\max}\left[C_t^{t_0}(x_t)\right] = \frac{1}{\lambda_{\min}\left[C_{t_0}^t(x_0)\right]} = \frac{1}{\lambda_{\min}\left[C_{t_0}^t(F_t^{t_0}(x_t))\right]}, \tag{13}$$

which leads to formula (7), as claimed, after substitution into (8). Note that (13)—and hence (7)—could not have been concluded immediately, because $\left[C_t^{t_0}(x_t)\right]^{-1} \neq C_{t_0}^t(x_0)$, as seen from (11). □

B. The case of two-dimensional flows

Most applications of LCS analysis in the literature have involved two-dimensional fluid flows with a simulated or experimentally measured velocity field $v(x, t)$. For such flows, the smallest FTLE can be expressed in terms of the largest FTLE and the determinant of the deformation gradient $DF_{t_0}^t$. Based on this fact, *Proposition 1* can be rewritten for two-dimensional flows as follows:

Proposition 2: For two-dimensional dynamical systems, we have

$$\Lambda_t^{t_0}(x_t) = \Lambda_{t_0}^t(F_t^{t_0}(x_t)) - \frac{1}{|t - t_0|}\int_{t_0}^t \mathrm{div} v(F_t^s(x_t), s)ds, \tag{14}$$

with div referring to the spatial divergence operator. In particular, for area-preserving two-dimensional flows, we have

$$\Lambda_t^{t_0}(x_t) = \Lambda_{t_0}^t(F_t^{t_0}(x_t)). \tag{15}$$

Proof: Note that by (3), we have

$$\det C_{t_0}^t(x_0) = \left[\det DF_{t_0}^t(x_0)\right]^2,$$

so for two-dimensional dynamical systems ($n = 2$), formula (7) can be rewritten as

$$\begin{aligned} \Lambda_t^{t_0}(x_t) &= -\Gamma_{t_0}^t(F_t^{t_0}(x_t)) \\ &= -\frac{1}{|t - t_0|}\log\sqrt{\lambda_{\min}\left[C_{t_0}^t\left(F_t^{t_0}(x_t)\right)\right]} \\ &= -\frac{1}{2|t - t_0|}\log\frac{\det C_{t_0}^t(x_0)}{\lambda_{\max}\left[C_{t_0}^t(x_0)\right]} \\ &= -\frac{1}{2|t - t_0|}\log\frac{\left[\det DF_{t_0}^t(x_0)\right]^2}{\lambda_{\max}\left[C_{t_0}^t(x_0)\right]} \\ &= \Lambda_{t_0}^t(x_0) - \frac{1}{|t - t_0|}\log\det DF_{t_0}^t(x_0), \end{aligned} \tag{16}$$

where we have used the fact that the flow map is an orientation-preserving diffeomorphism, and hence $\det DF_{t_0}^t(x_0) > 0$. By Liouville's theorem (Arnold[1]), we have

$$\det DF_{t_0}^t(x_0) = \exp\left[\int_{t_0}^t \mathrm{div} v(x(s, t_0, x_0), s)ds\right], \tag{17}$$

thus (16) and (17) together prove formula (14).

If, in addition, the two-dimensional dynamical system is area-preserving [e.g., $v(x, t)$ is a two-dimensional incompressible fluid velocity field], then $\mathrm{div} v \equiv 0$ leads to the surprisingly simple result (15). □

C. Implications for finding LCSs

Proposition 1 implies that we can simply locate ridges of the largest backward-time FTLE field, $\Lambda_t^{t_0}(x_t)$, by graphing $-\Gamma_{t_0}^t(x_0)$ over the corresponding advected locations $x_t = F_{t_0}^t(x_0)$, then finding the ridges of the resulting scalar field. This implies that attracting LCSs at time t should be marked by *troughs* of $\Gamma_{t_0}^t(F_t^{t_0}(x_t))$. Applying Proposition 1 in backward time gives that repelling LCSs at time $-t$ are marked by troughs of $\Gamma_{t_0}^{-t}(F_{-t}^{t_0}(x_{-t}))$.

For two-dimensional incompressible flows, formula (15) of Proposition 2 enables a simplified, unidirectional calculation of LCSs based on the largest FTLE field only: (1) ridges of the $\Lambda_{t_0}^t$ field graphed over initial trajectory positions x_0 reveal repelling LCSs at time t_0 (2) ridges of the same field graphed over final trajectory positions x_t reveal attracting LCSs at t. Similar statements hold in backward time.

While the initial positions x_0 are typically launched from an evenly spaced regular grid at time t_0, the trajectory positions x_t may be located along a strongly deformed grid. As a result, ridge extraction for $\Lambda_t^{t_0}(x_t)$ may be numerically challenging for large deformations of the grid, i.e., for large times t. A way to address this challenge is to first interpolate the scattered values $\Lambda_t^{t_0}(x_t)$ over to a regular grid of positions $\tilde{x}_t$, then extract ridges of $\Lambda_t^{t_0}(\tilde{x}_t)$.

IV. EXAMPLES

Here we consider three two-dimensional numerical examples to illustrate our results. Higher-dimensional examples appear to be more challenging to handle due to the large deformations in the grid of advected initial conditions. For this reason, we relegate the numerical illustration of Proposition 1 on higher-dimensional problems to future work.

A. The forced Duffing equation

Consider the forced Duffing oscillator

$$\dot{x}_1 = x_2,$$
$$\dot{x}_2 = x_1 - x_1^3 + \varepsilon \sin t.$$

This system is an area-preserving two-dimensional dynamical system, and hence Eq. (15) applies. We select the forcing amplitude $\varepsilon = 0.1$ to ensure the existence of a small-amplitude hyperbolic periodic orbit that perturbs from the saddle point $x_1 = x_2 = 0$ of the steady limit. Below we use FTLE to locate the stable manifold (a repelling LCS) and the unstable manifold (an attracting LCS) of the periodic orbit.

First, for reference, we locate the unstable manifold at $t = 10$ in the standard way, i.e., by determining the ridges of the largest FTLE field $\Lambda_t^{t_0}$, computed from $t = 10$ back to $t_0 = 0$ with time step $\Delta t = 0.01$. This computation is performed over an initial grid consisting of 800×600 points uniformly distributed in the domain $[-2, 2] \times [-1.5, 1.5]$. For trajectory integration, we use the fourth order Runge–Kutta method to obtain the forward-time FTLE field shown in Fig. 1(a).

Next, we compute the largest FTLE field $\Lambda_{t_0}^t(x_0)$ for a similar grid of points x_0 initialized at $t_0 = 0$, then advected forward up to time $t = 10$ using the same $\Delta t = 0.01$. To test formula (15), we plot the FTLE values $\Lambda_{t_0}^t(x_0)$ over the current positions $x_t = x(t, t_0, x_0)$ at time $t = 10$. In the interest of better visualization, we follow the numerical procedure proposed in Sec. III C above, i.e., interpolate the FTLE field $\Lambda_{t_0}^t(F_t^{t_0}(x_t))$ from the deformed grid of current positions x_t onto a regular grid of positions $\tilde{x}_t$ using Delaunay triangulation.[3] The computational cost of this process is small: for the resolution used, the triangulation took a few seconds (less than 1% of the total computational time). The results are shown in Fig. 1(b).

In agreement with formula (15), the LCSs emerging from Figs. 1(a) and 1(b) are identical. Note that in Fig. 1(b), some points of the domain have no associated FTLE values shown (upper-left and lower-right corners). This is because the number of advected points at these locations is not sufficiently large to yield meaningful interpolated values for the FTLE field.

In Fig. 1(c), we show the stable manifold of the hyperbolic periodic orbit at time $t_0 = -10$. The stable manifold forms a ridge of the largest FTLE field $\Lambda_{t_0}^t(x_0)$ computed by advecting a 800×600 initial grid from $t_0 = -10$ to $t = 0$. In Fig. 1(d), the same manifold is computed by applying formula (15) in backward time, i.e., by plotting the backward FTLE field $\Lambda_t^{t_0}(x_t)$ over points $\tilde{x}_0$ of a regular grid, interpolated from FTLE values obtained over the advected positions $x_0 = F_t^{t_0}(x_t)$. Again, the LCSs obtained from the two different computations agree, as stated in Proposition 1.

B. Forced-damped Duffing equation

Next, we illustrate the validity of the more general formula (14) of Proposition 2 that applies to nonarea-preserving flows as well. We consider the forced-damped Duffing oscillator

$$\dot{x}_1 = x_2$$
$$\dot{x}_2 = x_1 - x_1^3 - 025x_2 + 04\cos t,$$

with the constant divergence $\mathrm{div} v = -0.25$. For this choice of parameters, the systems admits a homoclinic tangle formed by the stable and unstable manifolds of a saddle-type periodic orbit (Guckenheimer and Holmes[4]).

We first locate the unstable manifold (attracting LCS) of the hyperbolic periodic orbit near the origin at time $t = 0$ in the standard way, i.e., as a ridge of the largest FTLE field computed from $t_0 = 0$ back to $t = -5$ on the same grid and with the same numerical method and time step as in the previous example [see Fig. 2(a)]. To test formula (14), we also locate the same manifold by (1) computing the FTLE field $\Lambda_t^{t_0}(x_t)$ from $t = -8$ to $t_0 = 0$; (2) subtracting the integrated divergence of the velocity field along the trajectories as given in (14); (3) interpolating the value of $\Lambda_t^{t_0}(F_{t_0}^t(x_0))$ obtained from (14) to a regular 800×600 grid of points $\tilde{x}_0$ at t_0 using Delaunay triangulation; (4) plotting $\Lambda_t^{t_0}(F_{t_0}^t(\tilde{x}_0))$ in Fig. 2(b). Note again that the results in Figs. 2(a) and 2(b) are identical, with the exception of small corner areas of the grid where the interpolation fails, as earlier. In Fig. 2(c), we show the field $\Lambda_t^{t_0}(F_{t_0}^t(x_0))$ without interpolation in order to highlight the importance of this step in the computational procedure for longer integration times.

We omit here a similar comparison of the two sides of (14) for the stable manifold, which again gives identical results.

C. Forced-damped Duffing–van der Pol equation

As a third example, we study a combination of a Duffing and a van der Pol oscillator of the form,

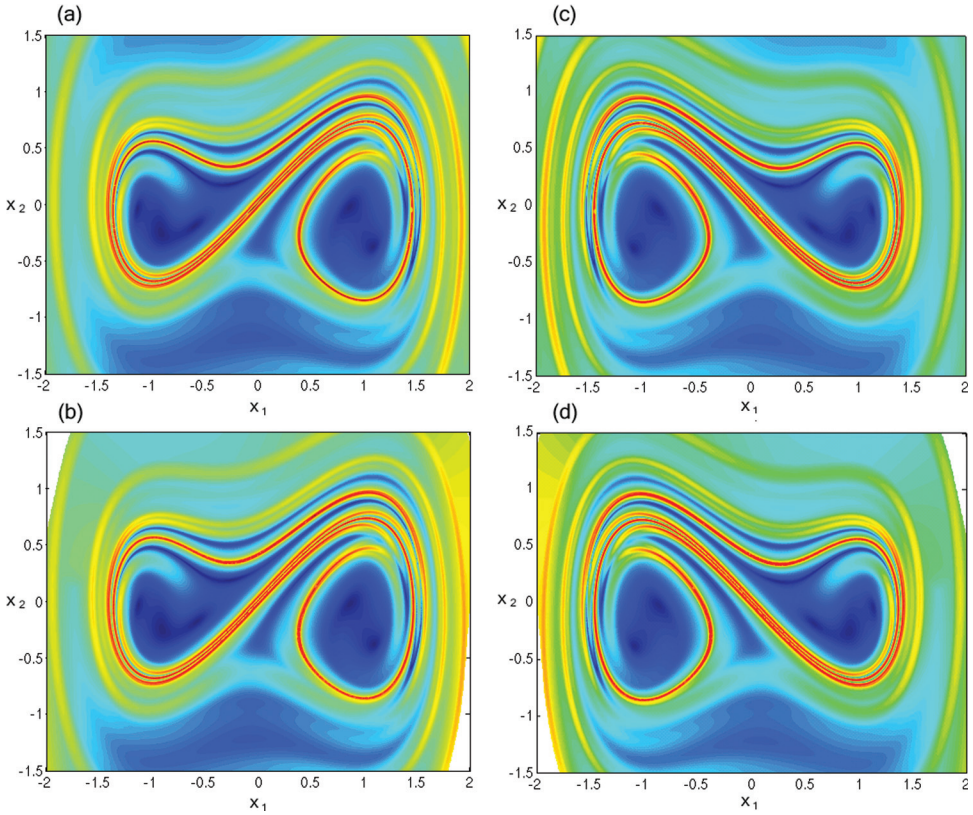

FIG. 1. (Color online) (a) Unstable manifold (attracting LCS) of the forced Duffing equation from a standard backward FTLE calculation (b) same from a forward FTLE calculation using formula (15). (c) Stable manifold (repelling LCS) for the same system from a standard forward FTLE calculation (d) same from a backward FTLE calculation using formula (15).

$$\dot{x}_1 = x_2,$$
$$\dot{x}_2 = x_1 - x_1^3 + 05x_2\left(1 - x_1^2\right) + 01\sin t.$$

This system admits an attracting two-dimensional torus (due to the van der Pol term) that encircles a homoclinic tangle arising from the Duffing-type term. The homoclinic tangle is formed by the stable and unstable manifolds of a small-amplitude periodic orbit near the origin. In this example, the smallest FTLE field turns out to yield better images of the attractor than the largest FTLE.

In Fig. 3(a), we show the unstable manifold (attracting LCS), identified in the standard way, i.e., as a ridge of the backward FTLE field computed from $t=6$ back to $t_0=0$ with $\Delta t = 0.01$. Observe that the strong attraction to the torus results in a rapid divergence of backward-time trajectories, suppressing the unstable manifold of the periodic orbit in the FTLE calculation. (We show no color where the numerical integration we used blew up.) By contrast, Fig. 3(b) shows the results obtained from the application of formula (14), with the forward FTLE field computed from $t_0=0$ to $t=6$ with the same time step. This example illustrates that in case of strong instabilities in a given time direction, using the smallest FTLE in the other time direction may give a more balanced view of all LCSs present in the system.

D. Experimental flow field around a jellyfish

In this final example, we illustrate the most general form of our results, Eq. (7), on an experimental velocity field obtained from particle image velocimetry (PIV) measurements near a swimming jellyfish. Details of this experiment can be found in Ref. 12.

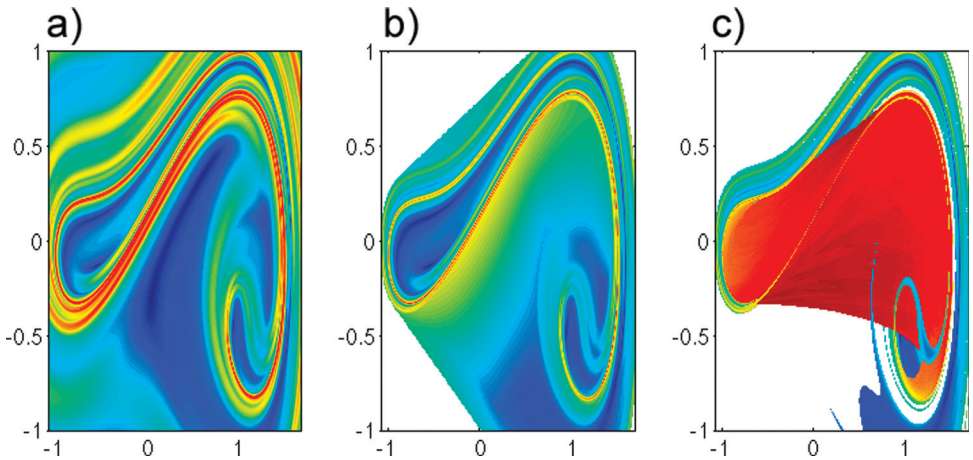

FIG. 2. (Color online) (a) Unstable manifold (attracting LCS) of the forced-damped Duffing equation from a standard backward FTLE calculation (b) same from a forward FTLE calculation using (14) (c) same as (b) but without interpolating $\Lambda_t^{t_0}(F_{t_0}^t(x_0))$ over a regular grid of positions.

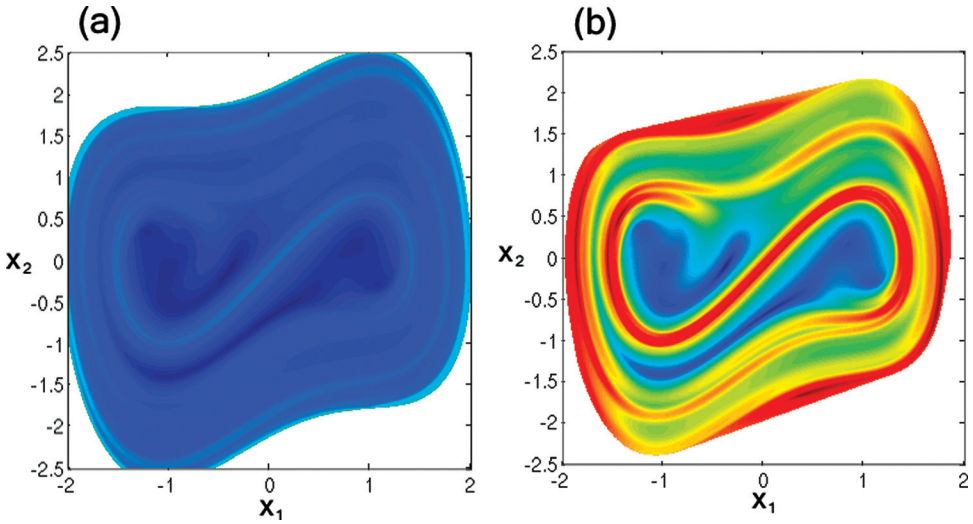

FIG. 3. (Color online) (a) Unstable manifold (attracting LCS) of the forced-damped Duffing–van der Pol oscillator, obtained from a standard backward FTLE calculation. (b) The same attracting LCS obtained from a forward FTLE calculation using formula (14).

Figure 4(a) shows attracting LCS candidates identified as ridges of the largest FTLE field $\Lambda^t_{t_0}(x_0)$, which is computed by advecting points x_0 backward from an initial grid of 600×600 points. For advection, we used a fourth order Runge–Kutta scheme with integration time step $\Delta t = 0.005$, and with linear interpolation applied in time and space to the experimental velocity field.

In Figs. 4(b)–4(e), we illustrate formula (7) by comparing the largest FTLE field $\Lambda^t_{t_0}(x_0)$ with the smallest FTLE field $-\Gamma^{t_0}_t(F^t_{t_0}(x_0))$ computed over the advected grid $F^t_{t_0}(x_0)$ for different integration parameters. More specifically, in Fig. 4(b), we use a 600×600 grid, $\Delta t = 0.005$, and cubic interpolation in time and space. In Fig. 4(c), we perform the same computation but on a smaller, 300×300 grid. We observe that the reduction of the number of points has no visible impact on the quality of the computed field. Similarly, an increase in the time step to $\Delta t = 0.01$ has an unnoticeable effect in Fig. 4(d). Changing the interpolation scheme from cubic to linear, using the smaller 300×300 grid, and increasing the time step to $\Delta t = 0.01$ simultaneously lead to a slight degradation in the of the plot quality [cf. Fig. 4(e)]. Keeping the same time step but decreasing the grid resolution even further to 100×100 makes the plot somewhat blurred [cf. Fig. 4(f)], but the LCS candidates remain well-defined and virtually identical.

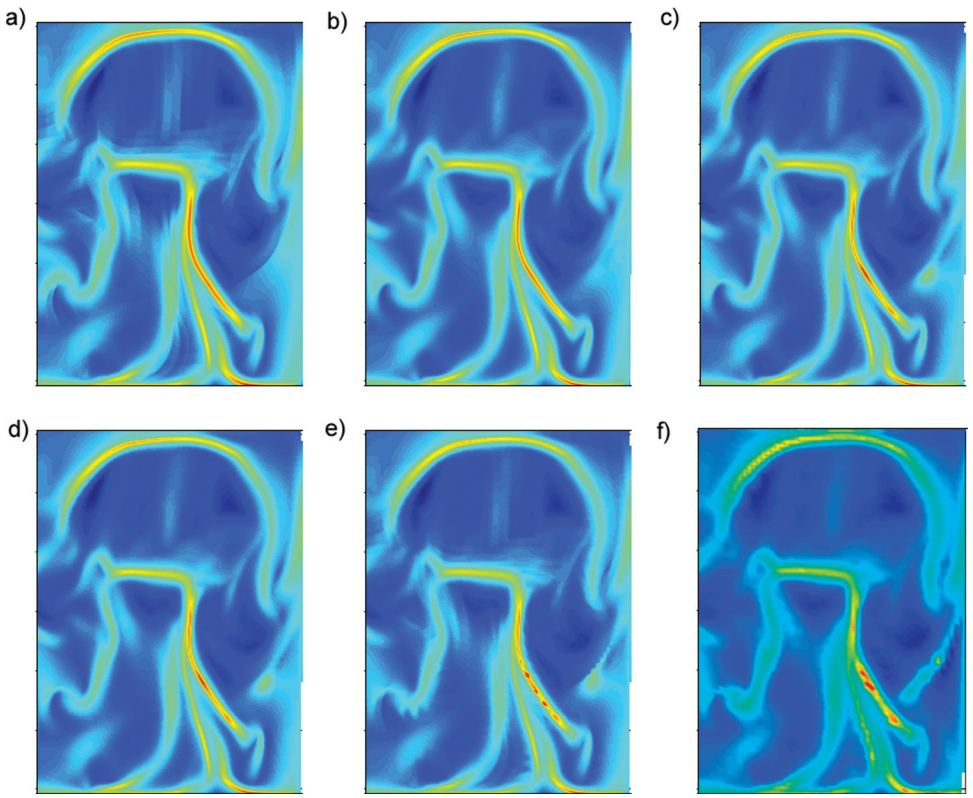

FIG. 4. (Color online) (a) Attracting LCSs for the experimentally measured flow field around a jellyfish from the largest FTLE field with $\Delta t = 0.005$, linear interpolation in time and space, and grid resolution 600×600. (b) Attracting LCSs obtained from Eq. (7) for step size $\Delta t = 0.005$, cubic interpolation in time and space, and grid resolution 600×600. (c) Attracting LCSs obtained from Eq. (7) for, but with $\Delta t = 0.005$, cubic interpolation in time and space, and resolution 300×300. (d) Attracting LCSs obtained from Eq. (7) for $\Delta t = 0.01$, cubic interpolation in time and space, resolution 300×300. (e) Attracting LCSs obtained from Eq. (7) for $\Delta t = 0.01$, linear interpolation in time and space, resolution 300×300. (f) Attracting LCSs obtained from Eq. (7) for $\Delta t = 0.01$, linear interpolation in time and space, resolution 100×100.

V. CONCLUSIONS

In this note, we have pointed out that the smallest FTLE field can be used to extract attracting LCSs from forward-time trajectories and repelling LCSs from backward-time trajectories. We have illustrated this observation on two-dimensional, nonautonomous area-preserving and dissipative dynamical systems, as well as on the experimentally measured flow field around a jellyfish. Beyond establishing a relationship between LCSs and the smallest FTLE for the first time, our results allow for computational savings over the standard LCS extraction method that requires trajectory integration in both time directions. In addition, as our third example above shows, using the smallest FTLE for LCS analysis is more accurate if computing the largest FTLE leads to rapidly growing instabilities.

We believe that the simple relationship between the smallest FTLE and LCSs pointed out here also makes LCS analysis more readily applicable to problems involving real-time flow analysis. In particular, as one gathers more and more velocity data at increasing times t, a single forward-running calculation reveals the attracting LCSs at time t. This, for instance, enables the real-time tracking of the present (time t) center of material accumulation, while revealing in more and more detail the original partition of the phase space by repelling LCSs at t_0 that has lead to the current distribution of initial conditions.

ACKNOWLEDGMENTS

We are grateful to Jeff Peng for providing us with the experimental data set for our jellyfish example in Sec. IV D. We would also like to thank the anonymous reviewers for their useful remarks and suggestions that have led to an improvement of this manuscript. Finally, we are grateful to Francesco Rizzi for pointing out a typo in the integration parameters used in Sec. IV A.

[1]Arnold, V. I., *Ordinary Differential Equations* (MIT Press, Cambridge, 1978).
[2]Brunton, S. L., and Rowley, C. W., "A comparison of methods for fast computation of time-varying FTLE fields," Chaos **20**, 017510 (2010).
[3]Edelsbrunner, H., *Algorithms in Combinatorial Geometry* (Springer-Verlag, New York, 1987).
[4]Guckenheimer, J., and Holmes, P., *Nonlinear Oscillations, Dynamical Systems, and Bifurcations of Vector Fields* (Springer-Verlag, New York, 1983).
[5]Haller, G., and Yuan, G., "Lagrangian coherent structures and mixing in two-dimensional turbulence," Physica D **147**, 352 (2000).
[6]Haller, G., "Distinguished material surfaces and coherent structures in three-dimensional fluid flows," Physica D **149**, 248 (2001).
[7]Haller, G., "Lagrangian coherent structures from approximate velocity data," Phys. Fluids A **14**, 1851 (2002).
[8]Haller, G., "A variational theory of Lagrangian coherent structures," Physica D **240**, 574 (2011).
[9]Lekien. F., Shadden, S. C., and Marsden, J. E., "Lagrangian coherent structures in n-dimensional systems," J. Math. Phys. **48**, 065404 (1–19) (2007).
[10]Lipinski, D., and Mohseni, K., "A ridge tracking algorithm and error estimate for efficient computation of Lagrangian coherent structures," Chaos **20**, 017504 (2010).
[11]Peacock, T., and Dabiri, J., "Introduction to Focus issue: Lagrangian Coherent Structures," Chaos **20**, 01750 (2010).
[12]Peng, J. and Dabiri, J. O., "Transport of inertial particles by Lagrangian Coherent Structures: applications to predator-prey interaction in jellyfish feeding," J. Fluid Mech. **623**, 75 (2009).
[13]Shadden, S. C., Lekien, F., and Marsden, J. E., "Definition and properties of Lagrangian coherent structures from finite-time Lyapunov exponents in two-dimensional aperiodic flows," Physica D **212**, 271 (2005).
[14]Tang, W., Chan, P.W., and Haller, G., "Lagrangian Coherent Structure analysis of terminal winds detected by LIDAR. Part II: Structure evolution and comparison with flight data," J. Appl. Meteor. Climatol. (submitted).